



Application and Evaluation of [^{99m}Tc]-Labeled Peptide Nucleic Acid Targeting *MicroRNA-155* in Breast Cancer Imaging

Yaqun Jiang, MD^{1,2}, Yongkang Gai, PhD^{1,2}, Yu Long, MD^{1,2}, Qingyao Liu, PhD^{1,2}, Chunbao Liu, MD, PhD³ , Yongxue Zhang, MD^{1,2}, and Xiaoli Lan, MD, PhD^{1,2} 

Abstract

It has been reported that dysregulation of *microRNA-155* expression and function is associated with tumorigenesis, growth, tumor subtypes, invasion, and poor survival rates. Peptide nucleic acid (PNA), an artificially synthesized nucleic acid mimic, has been applied for molecular diagnosis. In this study, a PNA sequence that undergoes complementary binding to *miR-155* was labeled with ^{99m}Tc to evaluate whether the tracer could visualize the expression of *miR-155* in breast cancer. Both antisense PNA (anti-PNA, fully complementary bound to human mature *miR-155*, referred to as “anti-PNA-155”) and mismatched PNA (referred to as “mis-PNA”) single strands containing 23-mer were synthesized. The relative expression of *miR-155* in MCF-7 cells and tumors was higher than that in MDA-MB-231 cells and tumors. Single-photon emission computed tomography (SPECT) scan showed that radioactivity mainly accumulated in kidney. MCF-7 tumors, but not MDA-MB-231 tumors, were clearly visualized after [^{99m}Tc]anti-PNA-155 injection. MCF-7 tumors were less visible when co-injected with 100-fold excess of anti-PNA-155 or injected with [^{99m}Tc]mis-PNA, which suggested specific binding. Biodistribution study results were consistent with SPECT imaging. We successfully demonstrated that [^{99m}Tc]anti-PNA-155 could visualize *miR-155* expression in vivo, suggesting it may be a promising probe applied in breast cancer.

Keywords

breast cancer, *miR-155*, peptide nucleic acid (PNA), ^{99m}Tc, molecular imaging

Introduction

MicroRNAs (miRNAs) are a newly discovered class of endogenous and small noncoding single-stranded RNAs of 20 to 24 nucleotides.¹ They can target specific messenger RNAs (mRNAs) and degrade them, regulating gene expression at the posttranscriptional level. They have been found to participate extensively in many physiological and pathological processes such as cell proliferation and growth, differentiation, apoptosis, and oncogenesis.² Over the past decade, numerous studies have shown that altered expression of *microRNA-155* (*miRNA-155*, *miR-155*) is related to cancer and other diseases, reflecting staging, progress, and treatment outcomes.³ Particularly, *miR-155* is reported to aberrantly express in breast cancer, lung cancer, and B-cell lymphoma.⁴⁻⁶ It is reported that *miR-155* may act as an oncogene or a tumor suppressor depending on its expression level.⁷ Acquiring the expression level of *miR-155* whenever necessary may help investigate cancer

progression, which is an appealing strategy for deciding treatment plans.

Numerous studies have supported that miRNAs obtained from tissues and body fluid play a promising role in cancer detection.⁸ It is vital to develop noninvasive detection techniques for human cancer and other diseases in living subjects.

¹ Department of Nuclear Medicine, Union Hospital, Tongji Medical College, Huazhong University of Science and Technology, Wuhan, China

² Hubei Province Key Laboratory of Molecular Imaging, Wuhan, China

³ Department of Nuclear Medicine, the Central Hospital of Wuhan, Tongji Medical College, Huazhong University of Science and Technology, Wuhan, China

Submitted: 27/10/2019. Revised: 17/01/2020. Accepted: 14/02/2020.

Corresponding Author:

Xiaoli Lan, Department of Nuclear Medicine, Wuhan Union Hospital, No. 1277 Jiefang Ave, Wuhan, 430022, China.

Email: LXL730724@hotmail.com



The visualization of *miR-155* expression in vivo can help to tailor treatment schemes because its overexpression is related to genome instability and resistance to therapy. An in vivo study by Van Roosbroeck et al⁹ showed that application of anti-*miR-155* treatment could make *miR-155*-overexpressing tumors sensitive to cisplatin chemotherapy in an orthotopic lung cancer model, leading to an obvious decrease in tumor size. Therefore, it is necessary to develop a molecular probe targeting *miR-155*, to allow visualization and semi-quantitation of the expression of *miR-155* in vivo with positron emission tomography (PET) or single-photon emission computed tomography (SPECT).

The third-generation antisense oligonucleotides (ASONS) such as peptide nucleic acid (PNA), locked nucleic acid, and phosphoramidate morpholino were developed.¹⁰ Comparing to normal oligonucleotides, PNAs hybridize more specifically and strongly to RNA and DNA.¹¹ In addition, PNAs resist both nucleases and proteases. They not only don't interact with cellular proteins which often normally bind with negatively charged macromolecules but also don't induce RNase degradation of bound miRNA or mRNA.¹² In addition to their application in molecular imaging, ASONS were first proposed primarily as therapeutic agents.¹³ Therefore, ASONS and their analogues have been widely studied in molecular imaging and gene therapy with promising application.¹⁴

Antisense imaging has been widely and intensively studied as an important method for noninvasively imaging oncogene expression in vivo.¹⁵ Oligonucleotide analogues labeled with radionuclides, fluorophores, or contrast agents as markers for antisense imaging of oncogene mRNA are expected to have great potential for this.¹⁶ Tian et al¹⁷ designed and synthesized a [^{99m}Tc]chelator-PNA-peptide probe to hybridize with cyclin D1 (*CCND1*, encoding cyclin D1 protein) mRNA and showed that high levels of *CCND1* expression could be detected in vivo. Paudyal et al¹⁸ showed that ⁶⁴Cu-DOTA-PNA-peptide targeting human epidermal growth factor receptor 2 mRNA expression could reflect therapeutic efficacy or resistance sooner than computed tomography (CT) or magnetic resonance imaging (MRI). MicroRNAs, another widely studied target for antisense imaging, have been reported to play a key role in pathogenesis of various diseases such as cancer.¹⁹

In this study, we developed a [^{99m}Tc]-labeled antisense PNA probe targeting *miR-155* and evaluated its application in the visualization of *miR-155* expression using human breast cancer xenograft models.

Materials and Methods

Design and Synthesis of PNA Precursor

The antisense PNA was designed to complement the human mature sequence *hsa-miR-155-5p* (5'-UAAUGCUAAUCGU-GAUAGGGGUU-3', MIR155HG, MIMAT0000646) on the basis of the miRBase database.²⁰ The designed PNA sequence showed no gaps or mismatches when performed sequence alignment by Basic Local Alignment Search Tool among

human genomic plus transcript (Human G+T) and mouse genomic plus transcript (Mouse G+T). The antisense PNA (anti-PNA-155) (5'-ACCCCTATCACGATTAGCATTA-3'), targeting *miR-155* with highest specificity and affinity, and the mismatched PNA (mis-PNA) (5'-ACCCAATCGTCAAATTC-CATATA-3'),²¹ which was chosen to interact with none of the human genes, were synthesized and purified.

For ^{99m}Tc labeling, a short peptide consisting of 4 amino acids (Gly-(D)-Ala-Gly-Gly) which can form a N₄ structure was added at the 5' end as a linker for the coupling of ^{99m}Tc by the ligand exchange method. For the purpose of decreasing steric hindrance, a 4-aminobutyric acid was introduced.²² Both antisense and mismatched PNA precursors were commissioned by Shanghai Science Peptide Biological Technology Co, Ltd (Shanghai, China) for synthesis and purification.

Radiolabeling

Radiolabeling was performed referring to the method of Zhao et al.²² In brief, 10 μ L NaOH (0.15 M) was added to the PNA solution (1.7 nmol, 20 μ L) and mixed. Subsequently, 200 μ L (148-185 MBq) fresh [^{99m}Tc]-pertechnetate and 10 μ L SnCl₂·2H₂O (1 mg/mL, 0.01 M HCl) were added immediately in sequence. The mixture was then reacted for 45 minutes at 37°C. At the end of reaction, phosphate-buffered saline (PBS, pH 7.0, 1 \times) was added for dilution, and the final pH was approximately 7.0. Afterward, the reaction mixture was subjected to high-performance liquid chromatography (HPLC) for analysis using a 4.6 \times 250 mm Ultimate XB-C18 column (Welch Materials, Inc, Shanghai, China). High-performance liquid chromatography was performed on LC-20AT (Shimadzu Corporation, Tokyo, Japan) equipped with a SPD-20A UV/VIS detector and a flow count radiation detector (Bioscan, Washington, DC). The column was eluted at a flow rate of 1 mL/min at 25°C with a gradient of 5% to 90% MeCN/H₂O with 0.1% trifluoroacetic acid for 20 minutes monitoring at 260 nm.

In Vitro Stability and Partition Coefficient of Probes

Aliquots of [^{99m}Tc]anti-PNA-155 and [^{99m}Tc]mis-PNA were incubated in saline and fresh human serum at 37°C for 6 hours. Saline samples were subjected to analysis after incubation for 6 hours. Serum samples were mixed with an equal volume of anhydrous acetonitrile and then the mixture was centrifuged (13 000 g, 10 minutes) to precipitate plasma protein. The supernatant was then aspirated for HPLC analysis. The radiochemical purity of the samples was measured by HPLC under the above conditions.

Both 1.0 mL PBS (pH 7.4) and 1.0 mL 1-octanol were mixed in a 4-mL centrifuge tube. Then, [^{99m}Tc]anti-PNA-155 (370 kBq) and [^{99m}Tc]mis-PNA (370 kBq) were respectively added to the mixed solution. The mixture was then continuously vortexed for 4 minutes and centrifuged (4000 rpm, 5 minutes). Radioactivity counts of a 50 μ L sample from each phase was measured by an automatic gamma counter (PerkinElmer WIZARD2 2470, Spokane, Washington). The partition

Table 1. The Primer Sequences Involved in This Study.

Gene Name	Primer Name	Primer Sequences (5'-3')
Reverse transcription primer	RT- <i>hsa-miR-155-5p</i>	GTCGTATCCAGTGCAGGGTCCGAGGTATTGCGACTGGATACGACaccct
Forward primer	<i>hsa-miR-155-5p</i> -F	GGCCGTTAATGCTAATCGTGATA
Reverse primer	RP2	CAGTGCAGGGTCCGAGGTAT
Reverse transcription primer	RT-U6-2	CGAATTTGCGTGTCTATCCT
Forward primer	U6-2-F	CTCGCTTCGGCAGCACATA
Reverse primer	U6-2-R	CGAATTTGCGTGTCTATCCT

coefficient was calculated as follows: $\text{Log } P = \text{Log}_{10} (\text{counts in 1-octanol}/\text{counts in PBS})$.

Metabolism

Four normal BALB/c nude mice (8 weeks old, female) were used to evaluate the metabolic stability of [^{99m}Tc]anti-PNA-155 and [^{99m}Tc]mis-PNA. Each mouse was injected via tail vein with the radiotracers (55.5-74 MBq). A sufficient amount of urine sample was collected at 2 hours postinjection and was mixed with double volume of acetonitrile. The mixtures were centrifuged at 13 000g for 10 minutes. The supernatant was diluted and analyzed by radio-HPLC.

Cell Culture

The human breast cancer cell lines MCF-7 and MDA-MB-231 were purchased from the Type Culture Collection of the Chinese Academy of Sciences (Shanghai, China). They were both cultivated in Dulbecco's modified Eagle high-glucose medium (DMEM; Gibco, Carlsbad, California) at 37°C in a humidified incubator with 5% CO₂. The medium was supplemented with 10% fetal bovine serum (Gibco), 100 µg/mL streptomycin, and 100 U/mL penicillin (Solarbio, Shanghai, China).

Quantitative Real-Time Polymerase Chain Reaction

Total RNA was extracted from MCF-7 and MDA-MB-231 cells and tumor tissues using NucliSens easyMAG extraction systems following the manufacturer's instructions (bioMérieux, Inc, Durham North Carolina). Extracts were stored at -80°C for no longer than 1 week until use. All the primers are summarized in Table 1. Subsequently, an miRNA fluorescent quantitative polymerase chain reaction detection kit (BaiAoLaiBo, Haidian, Beijing, China) was introduced to test *miR-155* in cells and tumor tissues. U6 was applied as an internal control to normalize the expression levels of *miR-155*. Relative threshold cycle values were utilized to further analyze the results of quantitative real-time polymerase chain reaction (qRT-PCR), converting to fold changes.

In Vitro Cell Study

MCF-7 and MDA-MB-231 cells were collected at approximately 85% confluence. Then, cells were counted by a cytometer (Cellometer Mini; Nexcelom Bioscience LLC,

Lawrence, Massachusetts). Cells were seeded in 24-well plates (3 duplicate wells per each group) at the amount of 2×10^5 cells per well and cultured overnight. [^{99m}Tc]anti-PNA-155 (37 kBq, 50 µL) was added to each well and incubated at 37°C for 1, 2, 4, and 6 hours. For the control study, MCF-7 was used for uptake of [^{99m}Tc]mis-PNA. The supernatant and cell lysates were collected respectively at the end of incubation at each time point and their radioactivity was measured with a γ -counter.

The following blocking experiment was carried out using MCF-7 cells. One group of cells was incubated only with [^{99m}Tc]anti-PNA-155 (37 KBq, 50 µL) for 6 hours at 37°C. The other group was incubated with a 100-fold excess of non-labeled anti-PNA-155 30 minutes in advance and then incubated with [^{99m}Tc]anti-PNA-155 (37 KBq, 50 µL) for 6 hours at 37°C.

MCF-7 and MDA-MB-231 cells were subjected to cell internalization and efflux assays. For cell internalization study, [^{99m}Tc]anti-PNA-155 (37 KBq, 50 µL) was added to each well and incubated at 37°C for 1, 2, 4, and 6 hours. At the end of incubation, the supernatant was removed and collected and acetate-Hank's balanced salt solution (HBSS) (pH 4.0) was added and incubated at 37°C for 10 minutes. The supernatant and cells were collected and counted. For cell efflux study, [^{99m}Tc]anti-PNA-155 (37 KBq, 50 µL) was added and incubated at 37°C for 4 hours. Cell uptake at 4 hours was considered the zero point for efflux study. The supernatant of each well was collected after incubation for 4 hours. Then fetal bovine serum (FBS)-free DMEM medium was added and incubated for 1, 2, 4, and 6 hours. The remaining steps were the same as above. The cell uptake ratio was calculated as follows: $\text{cell uptake } \% = \frac{\text{counts of cells}}{\text{counts of supernatant} + \text{counts of cells}} \times 100\%$.

Animal Models

All animal experiments were carried out according to the Institutional Animal Care and Use Committee of Tongji Medical College of Huazhong University of Science and Technology. Female BALB/c nude mice (5-6 weeks old) were purchased from Beijing HFK Bioscience Co Ltd (Beijing, China) and were kept in a specific pathogen-free barrier system room. For breast cancer xenograft models, female BALB/c nude mice were inoculated subcutaneously in the right shoulder with a cell suspension of MCF-7 and MDA-MB-231 (1.0×10^7 , 125 µL), respectively. When tumor size reached 0.8 to 1.0 cm, the xenografted mice were subjected to following studies.

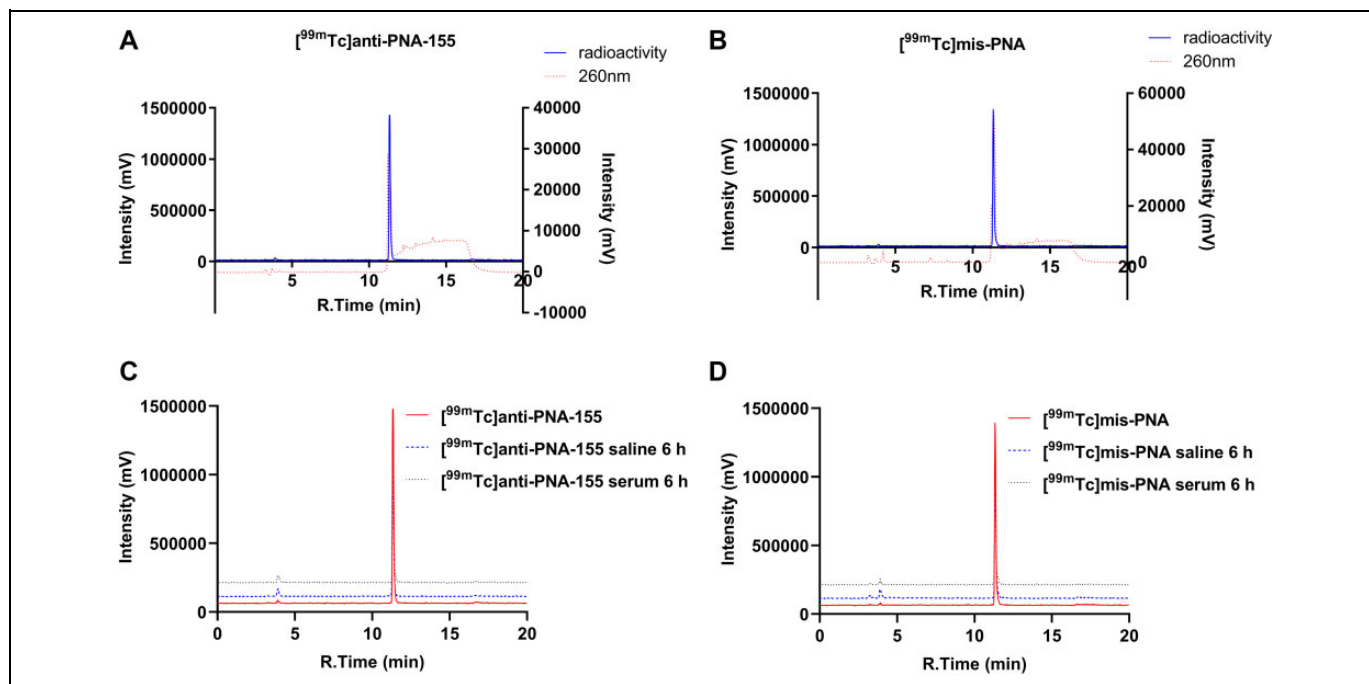


Figure 1. Identification and in vitro stability study of [^{99m}Tc]anti-PNA-155 (A) and [^{99m}Tc]mis-PNA (B), respectively. Analytic radio-HPLC chromatograms of [^{99m}Tc]anti-PNA-155 and [^{99m}Tc]mis-PNA, and the 6-hour in vitro stability of [^{99m}Tc]anti-PNA-155 (C) and [^{99m}Tc]mis-PNA (D) in saline and serum, respectively. The small peak at about 4 minutes represents free technetium. HPLC indicates high-performance liquid chromatography; PNA, peptide nucleic acid.

SPECT Imaging

The MCF-7 and MDA-MB-231 xenograft mice were injected via tail vein with [^{99m}Tc]anti-PNA-155 (11.1-13 MBq, 125 μL). SPECT scan was performed using a human SPECT (Symbia T6; Siemens, Erlangen, Germany) equipped with a dedicated pinhole collimator at 1, 2, 4, and 6 hours postinjection with an acquisition time of 15 minutes. Mice were anesthetized intraperitoneally with 1% sodium pentobarbital aqueous solution (0.1 mL/20 g mouse) and placed on the table in the prone position. For a control study, another group of MCF-7 xenograft mice ($n = 3$) were injected via tail vein with [^{99m}Tc]mis-PNA (11.1-13 MBq, 125 μL) and underwent SPECT scanning under the same conditions. Blocking experiments were performed in another group of MCF-7 tumor models ($n = 3$). The 100-fold excess of nonlabeled anti-PNA-155 was coinjected with [^{99m}Tc]anti-PNA-155 (11.1-13 MBq, 125 μL).

Biodistribution Studies

For biodistribution experiments, grouping was the same as with SPECT imaging. Either [^{99m}Tc]anti-PNA-155 (1.85 MBq/mouse) or [^{99m}Tc]mis-PNA (1.85 MBq/mouse) was injected via tail vein into each group of tumor xenografted mice ($n = 3$ in each group). The mice were euthanized 6 hours postinjection. Organs and tissues of interest were removed quickly and washed. All samples were weighed, and radioactivity was measured. The biodistribution result was

expressed as a percentage of the injected dose per gram of tissue (% ID/g). All radioactivity measurements were corrected for decay.

Statistical Analysis

Data are expressed as mean \pm standard deviation. Statistical analysis was performed using Student *t* test using commercial software (GraphPad Prism 8; GraphPad Software, La Jolla, California). $P < .05$ was considered a statistically significant difference.

Results

Chemical and Radiochemical Characterization of Probes

The molecular weights of anti-PNA-155 and mis-PNA were 6485.6 and 6468.1 g/mol determined by Matrix Assisted Laser Desorption Ionization-Mass Spectrometry (MALDI-MS) (Supplementary Figure S1). MALDI-MS (Shimadzu Biotech Axima Assurance, Shimadzu Biotech, Manchester, UK): *m/z* calcd for (N-term)G-dA-G-G-(g-aminobutyric acid)-acc cct atc acg att agc att aa(C-term) [M + 1], Found 6485.6; (N-term)G-dA-G-G-(g-aminobutyric acid)-acc caa teg tca aat tcc ata ta(C-term) [M + 1], Found 6468.1. The labeling process for [^{99m}Tc]anti-PNA-155 and [^{99m}Tc]mis-PNA was simple with a molar activity of 97.94 ± 8.89 GBq/ μmol ($n = 5$). The radioactivity yield and purity were $95.24 \pm 2.69\%$ and $93.62 \pm 3.85\%$, respectively ($n = 5$), as measured by analytic HPLC. The absorption peaks of anti-PNA-155 and mis-PNA at 260 nm were in line with their

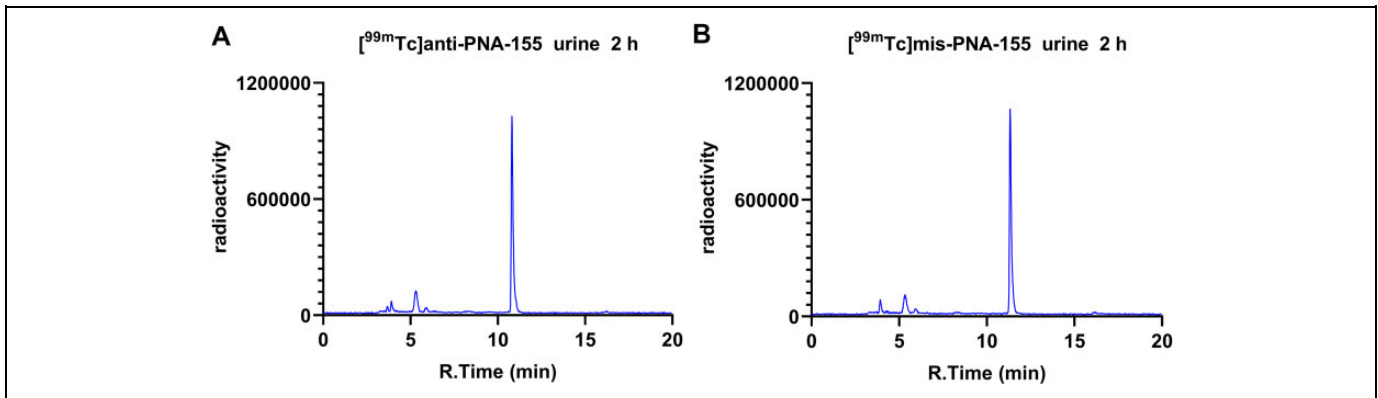


Figure 2. Analytic radio-HPLC chromatograms of [^{99m}Tc]anti-PNA-155 (A) and [^{99m}Tc]mis-PNA (B) in the urine at 2 hours postinjection. The peak at around 11.2 minutes is the intact [^{99m}Tc]-tracers. HPLC indicates high-performance liquid chromatography; PNA, peptide nucleic acid.

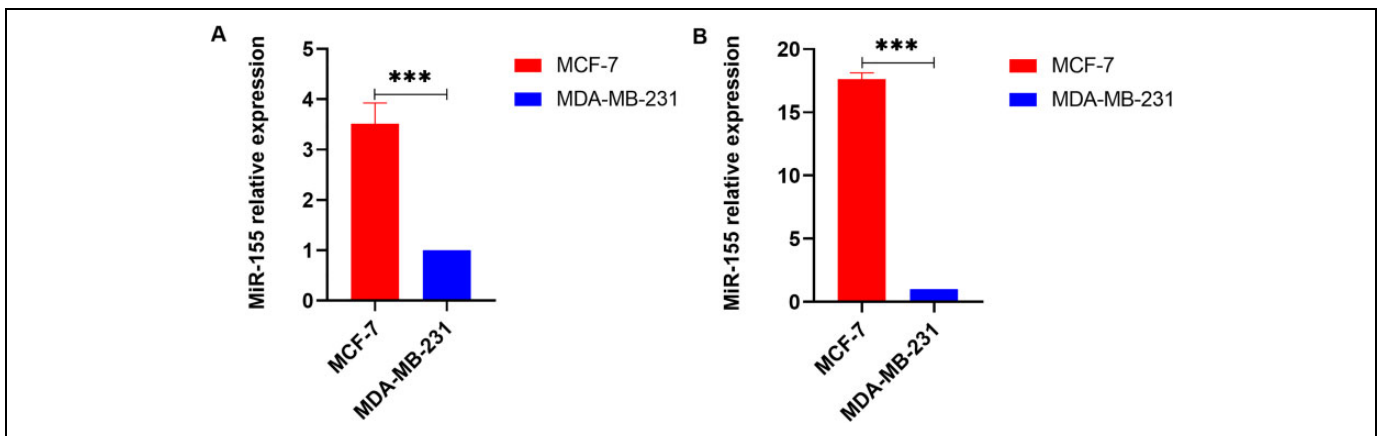


Figure 3. Quantitative real-time polymerase chain reaction was performed to evaluate the relative expression levels of *miR-155* by MCF-7 and MDA-MB-231 cells (A) and tumor tissues (B) ($n = 3$, mean \pm SD; *** $P < .001$). SD indicates standard deviation.

radiation peaks (Figure 1A and B). As shown in Figure 1C and D, the proportion of intact probes still exceeded 90% after incubation for 6 hours at 37°C in saline and serum, indicating good stability in vitro. The Log P of [^{99m}Tc]anti-PNA-155 and [^{99m}Tc]mis-PNA were -1.47 ± 0.02 and -2.00 ± 0.02 , respectively, indicating that the two probes are relatively water soluble and hydrophilic.

Metabolic Properties

Metabolism study of [^{99m}Tc]anti-PNA-155 and [^{99m}Tc]mis-PNA was conducted using normal BALB/c nude mice. Since both the probes are mainly excreted from renal, urine sample was collected and analyzed. As shown in Figure 2, the major radioactivity was still the intact [^{99m}Tc]-tracers, while they showed a certain degree of metabolism (around 15%) in urine sample at 2 hours postinjection.

Characterization of *miR-155* Expression in Cells and Tumor Tissues

A qRT-PCR assay was performed to characterize the expression of *miR-155* by MCF-7 and MDA-MB-231 cells and tumor

tissues. As can be seen from Figure 3, the relative expression level of *miR-155* by MCF-7 cells and tumor tissues was significantly higher than that of MDA-MB-231 ($P < .001$).

In Vitro Cell Studies

As shown in Figure 4A, the uptake of [^{99m}Tc]anti-PNA-155 by MCF7 cells increased gradually over time, and reached maximum at 6 hours, which was significantly higher than the uptake by MDA-MB-231 cells ($P < .001$). For control experiments, Figure 4B shows that the uptake of [^{99m}Tc]anti-PNA-155 was obviously higher than that of [^{99m}Tc]mis-PNA in MCF7 cells ($P < .001$). Cell-blocking studies were performed to assess the binding specificity of [^{99m}Tc]anti-PNA-155 in vitro. The uptake of [^{99m}Tc]anti-PNA-155 by another group of MCF7 cells decreased significantly when pretreated with excessive unlabeled anti-PNA-155 ($P < .001$) (Figure 4C). The cell internalization ratio of MCF-7 was much higher than MDA-MB-231 ($P < .001$; Figure 4D) and was similar to the cell uptake ratio of MCF-7. As shown in Figure 4E, the retention ratio of [^{99m}Tc]anti-PNA-155 in MCF-7 cells was obviously higher than that in MDA-MB-231 cells ($P < .001$).

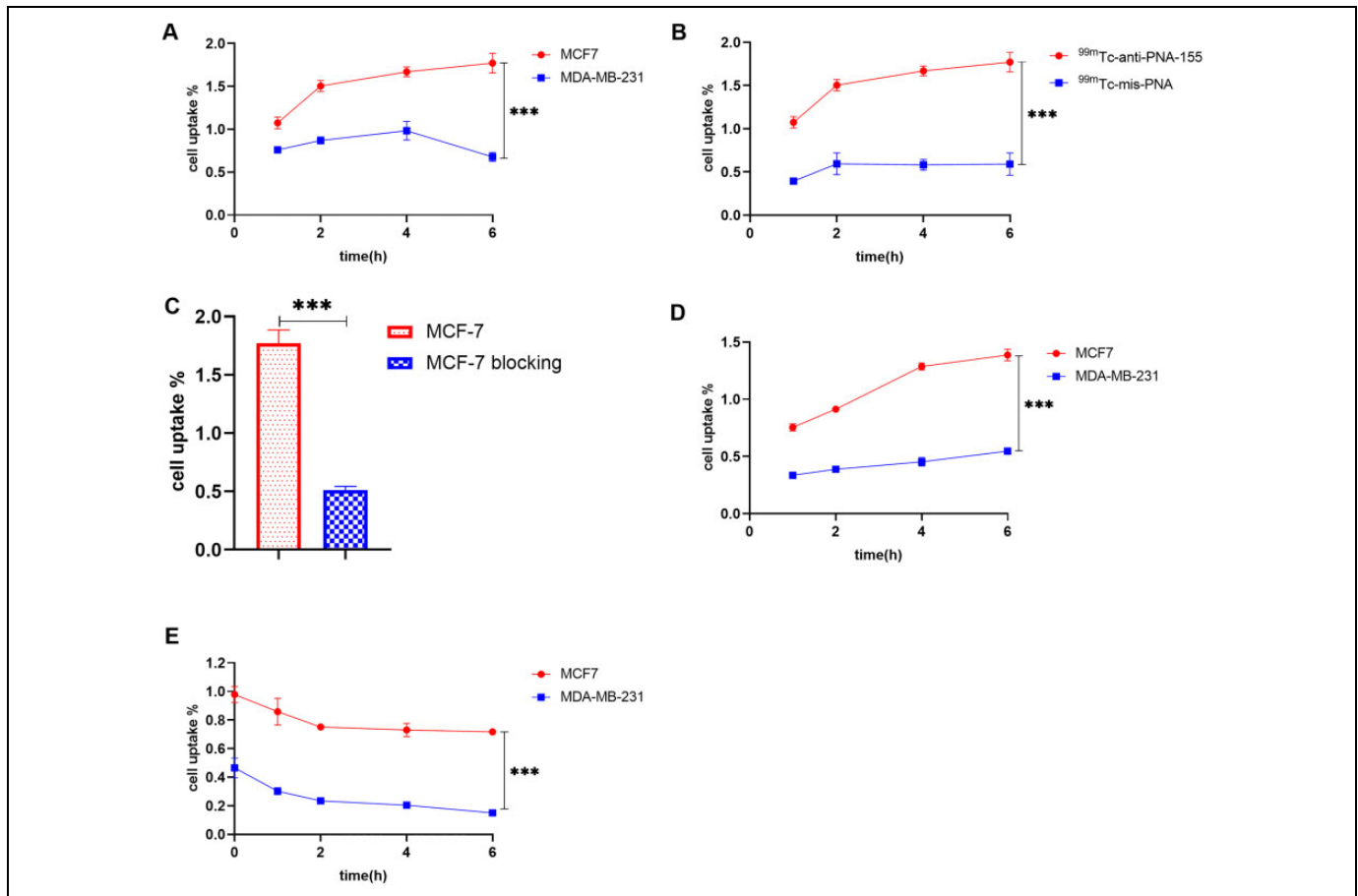


Figure 4. In vitro cell studies. The uptake of [^{99m}Tc]anti-PNA-155 in MCF-7 cells was higher than that in MDA-MB-231 cells (A). The uptake of [^{99m}Tc]anti-PNA-155 was higher than that of [^{99m}Tc]mis-PNA in MCF-7 cells at 6 hours (B). The uptake of [^{99m}Tc]anti-PNA-155 was blocked with unlabeled anti-PNA-155 in MCF-7 cells at 6 hours (C). Cell internalization (D) and cellular retention (E) of [^{99m}Tc]anti-PNA-155 in MCF-7 and MDA-MB-231 cells. Experiments were repeated 3 times with 3 duplicate wells set in each group. Data are expressed as mean \pm SD. *** $P < .001$. PNA indicates peptide nucleic acid; SD, standard deviation.

SPECT Imaging

SPECT scans were conducted to evaluate whether [^{99m}Tc]anti-PNA-155 could specifically visualize breast tumors with relative high expression levels of *miR-155*. As shown in Figure 5, radioactivity mainly accumulated in the abdomen and pelvis, which demonstrated that [^{99m}Tc]anti-PNA-155 and [^{99m}Tc]mis-PNA are metabolized mainly via kidney and liver. The contour of MCF-7 tumor was clearly visualized by [^{99m}Tc]anti-PNA-155 at 1, 2, 4, and 6 hours postinjection, while MDA-MB-231 tumor was not visible during the observation period (Figure 5A and B). For further determining the specificity of [^{99m}Tc]anti-PNA-155, blocking studies were conducted in another group of MCF-7 xenograft mice. The blocking studies showed that MCF-7 tumors were less visible and tumor uptake markedly decreased when blocked by excessive unlabeled anti-PNA-155 (Figure 5C). As control, MCF-7 tumors were less visualized by [^{99m}Tc]mis-PNA (Figure 5D).

Biodistribution Studies

Biodistribution studies were conducted in the xenografted mice to further evaluate pharmacokinetic characteristics as well as targeting affinity and specificity for *miR-155* in vivo of [^{99m}Tc]anti-PNA-155. The results of biodistribution are shown in Figure 6 and Supplementary Table S1. The highest radioactivity in the kidneys of MCF-7 (5.66 ± 0.99 %ID/g) and MDA-MB-231 (4.43 ± 0.21 %ID/g) indicated that renal clearance is the main metabolic pathway of [^{99m}Tc]anti-PNA-155, which is consistent with imaging findings. [^{99m}Tc]mis-PNA (6.31 ± 0.86 %ID/g in kidney) uptake was similar. The mean tumor uptake of [^{99m}Tc]anti-PNA-155 by MCF-7 xenograft mice (0.51 ± 0.05 %ID/g) was significantly higher than that by MDA-MB-231 (0.22 ± 0.02 %ID/g, $P = .0019$), which demonstrated the excellent ability to differentiate between tumors with relatively high and low expression level of *onco-miR-155*. The mean tumor uptake of [^{99m}Tc]anti-PNA-155 was higher than that of [^{99m}Tc]mis-PNA (0.38 ± 0.02 %ID/g, $P = .034$) in MCF-7 xenograft mice. In addition, when blocked

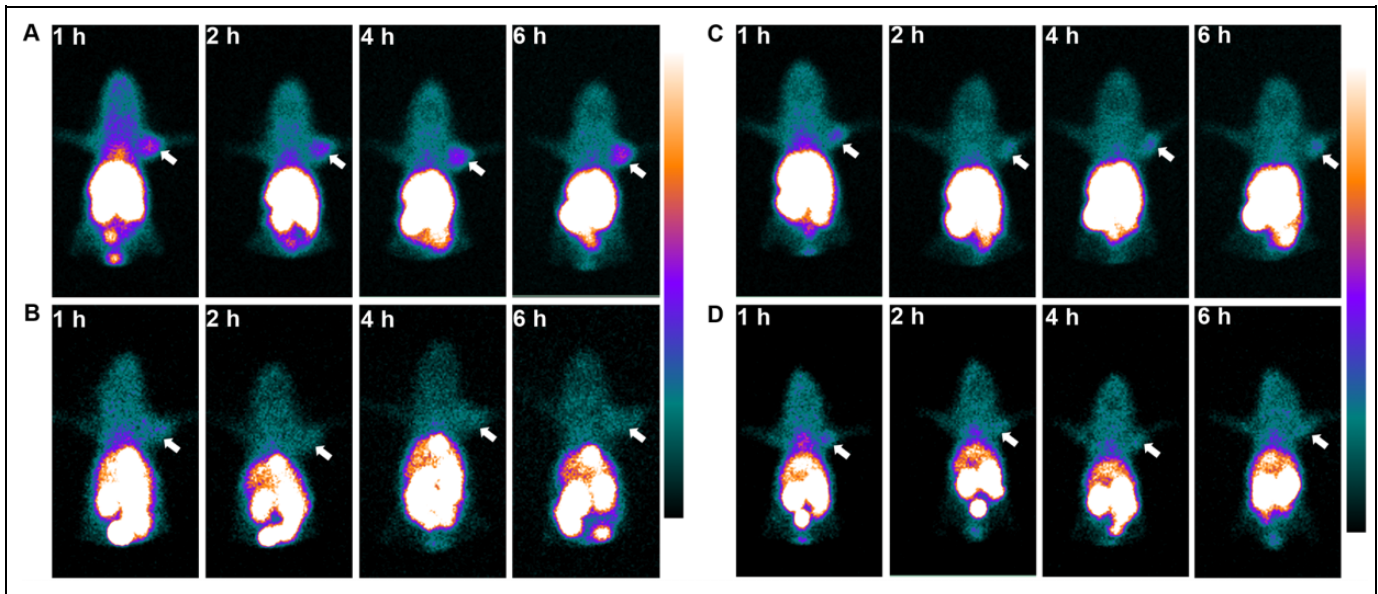


Figure 5. Representative static SPECT images of MCF7 (A) and MDA-MB-231 (B) tumor xenograft mice at 1, 2, 4, and 6 hours postinjection of [^{99m}Tc]anti-PNA-155, respectively. MCF-7 tumor-bearing mice were coinjected with unlabeled anti-PNA-155 and [^{99m}Tc]anti-PNA-155 and imaged at 1, 2, 4, and 6 hours (C). Images of MCF-7 tumor-bearing mice at 1, 2, 4, and 6 hours postinjection of [^{99m}Tc]mis-PNA (D). White arrows indicate the location of tumors. Each mouse was injected with probes of 11.1 to 13 MBq (300-350 μCi , 125 μL ; $n = 3$). PNA indicates peptide nucleic acid; SPECT, single-photon emission computed tomography.

with anti-PNA-155, the tumor uptake was significantly reduced ($0.34 \pm 0.04\% \text{ID/g}$, $P = .024$).

Discussion

Numerous studies have reported that dysregulation of miRNA expression level plays important roles in the progression of diseases including cardiovascular disorders,^{23,24} neurological disease,²⁵ diabetes,²⁶ and especially cancer.²⁷ Upregulation of the expression of *miR-155*, an oncogenic miRNA, is related to the development of breast cancer, which suggests its use as a potential tumor marker for breast cancer.²⁸ Based on their desirable properties, including that they are resistant to enzymatic degradation, hybridize more strongly and specifically to RNA, are stable over a wide range of pH, and display the highest melting temperature (T_m) for duplexes, PNAs are promising for development as antisense imaging agents.²⁹ In this study, we applied an antisense PNA probe specifically targeting *miR-155* to visualize its expression, thus providing some diagnostic and therapeutic information at the oncogene level for breast cancer.

The [^{99m}Tc]-labeled PNA antisense probe in our study was developed with a simple labeling process. It has a high radiochemical yield, high radiochemical purity, and good stability. The uptake by MCF-7 cells with their relatively higher expression of *miR-155* was significantly higher than by MDA-MB-231, indicating that [^{99m}Tc]anti-PNA-155 showed good targeting efficiency for *miR-155*. In addition, the uptake by MCF-7 cells of [^{99m}Tc]mis-PNA or of [^{99m}Tc]anti-PNA-155 blocked by unlabeled anti-PNA-155 was obviously reduced, showing good target specificity of [^{99m}Tc]anti-PNA-155 for *miR-155* in

vitro. Furthermore, the high retention ratio of [^{99m}Tc]anti-PNA-155 in MCF-7 cells indicated that [^{99m}Tc]anti-PNA-155 complementarily bound to *miR-155* in cytoplasm, thus reducing the probe efflux.

For in vivo SPECT imaging, MCF-7 tumors with relatively high *miR-155* expression were clearly visible, while MDA-MB-231 tumors with low *miR-155* expression were not visible after injection of [^{99m}Tc]anti-PNA-155 at all scan time points, indicating superior specificity and targeting capability of the probe. For biodistribution, the organs with the highest uptake of probe were kidney and liver, which is consistent with the studies of Mardirossian et al³⁰ and Sun et al.³¹ The uptake by MCF-7 tumor was obviously higher than MDA-MB-231 tumor postinjection of [^{99m}Tc]anti-PNA-155 at 6 hours. Consistent with the in vitro findings, the uptake by MCF-7 tumor of [^{99m}Tc]mis-PNA or of [^{99m}Tc]anti-PNA-155 when blocked by unlabeled anti-PNA-155 was low, again signifying that [^{99m}Tc]anti-PNA-155 specifically targets *miR-155*, and can visualize its expression in vivo.

It cannot be ignored that there are several shortcomings in this study. First, radioactivity in the blood was relatively high probably for the reasons that their hydrophobicity promotes PNA aggregation and seems to promote their relatively non-specific adherence to both other macromolecules and larger surfaces.³² Second, high uptake by kidney and liver resulted in high imaging background, mainly because the probe is mainly excreted by these organ systems. Finally, tumor uptake was relatively low due to unfavorable delivery efficiency of the probe, which is not conducive to imaging and further treatment. Tian et al²⁹ reported that tumor uptake was $0.20 \pm 0.05\% \text{ID/g}$ postinjection of [^{99m}Tc]MYC antisense probe at 24 hours. Tian

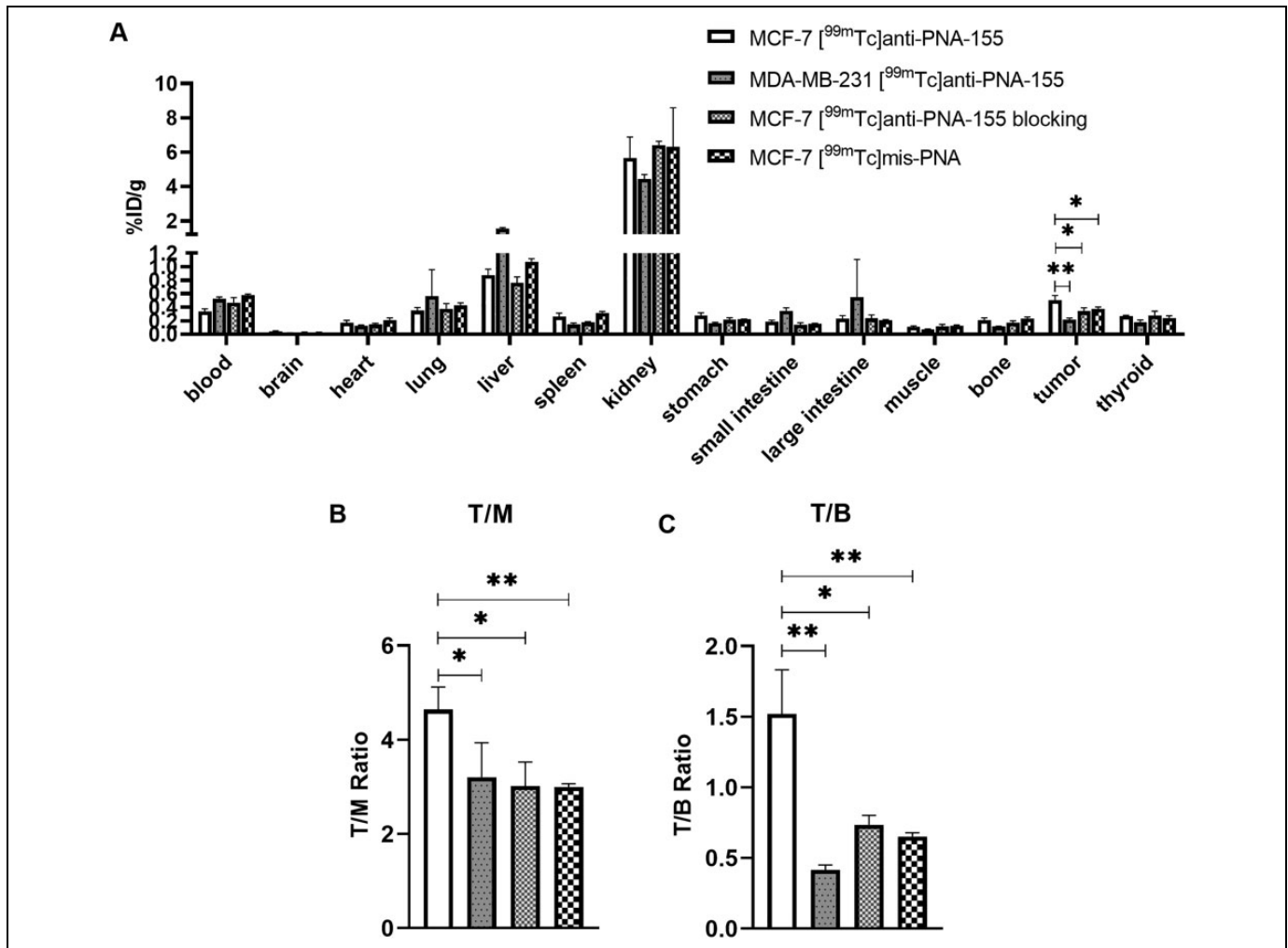


Figure 6. Biodistribution studies of [^{99m}Tc]anti-PNA-155 and [^{99m}Tc]mis-PNA in tumor xenograft mice. Tumor uptake comparison of [^{99m}Tc]anti-PNA-155 in MCF-7 tumors with or without coinjection of excess amount of unlabeled anti-PNA-155 at 6 hours postinjection (A). Differences of tumor to muscle (T/M) and tumor to blood (T/B) among each group are showed in (B) and (C). **P* < .05, ***P* < .01, ****P* < .001. Data are expressed as mean ± SD (*n* = 3). Each mouse was injected with probes of 1.85 MBq (50 μCi, 125 μL). PNA indicates peptide nucleic acid; SD, standard deviation.

et al¹⁷ developed [^{99m}Tc]CCND1-PNA-IGF1 chimeras with tumor uptake of 0.20 ± 0.06 %ID/g (4 hours), 0.17 ± 0.06 %ID/g (12 hours), and 0.11 ± 0.05 %ID/g (24 hours), respectively. Owing to PNA being a noncharged nucleotide analogue, the delivery of unmodified PNAs to target cells is less efficient.³³ Many strategies have been proposed to improve the delivery efficiency of PNAs. Chemical modifications were initially designed for conjugation to PNA to facilitate uptake such as cell-penetrating peptide R6-penetratin,³⁴ 4 lysine residues,³⁴ and octreotide.³⁵ Application of delivery carriers, such as gold nanoparticles,³⁶ cationic nanocomplexes,³⁷ cationic shell crosslinked nanoparticles,³⁸ liposomes,³⁹ and exosomes,⁴⁰ could improve the cell delivery efficiency of PNA and other nucleic acids.

Conclusion

In this study, we successfully prepared an antisense PNA-mediated probe and showed that [^{99m}Tc]anti-PNA-155 could

specifically and efficiently target oncogene *miR-155*, noninvasively visualizing *miR-155* expression in vivo, thus providing helpful information at gene level for breast cancer. However, relatively higher radioactivity in blood, lower delivery efficiency, and relatively low tumor uptake need to be improved in the future.


Declaration of Conflicting Interests

The author(s) declared no potential conflicts of interest with respect to the research, authorship, and/or publication of this article.

Funding

The author(s) disclosed receipt of the following financial support for the research, authorship, and/or publication of this article: This work was supported by the National Natural Science Foundation of China (No. 81630049, 81771863, and 81801738) and the Natural Science Foundation of Hubei Province (No. 2019CFB287).

ORCID iD

Chunbao Liu  <https://orcid.org/0000-0003-4600-9476>

Xiaoli Lan  <https://orcid.org/0000-0002-7263-7399>

Supplemental Material

Supplemental material for this article is available online.

References

- Reddy KB. MicroRNA (miRNA) in cancer. *Cancer Cell Int.* 2015;15:38.
- Trzybulska D, Vergadi E, Tsatsanis C. MiRNA and other non-coding RNAs as promising diagnostic markers. *EJIFCC.* 2018; 29(3):221–226.
- Jurkovicova D, Magyerkova M, Kulcsar L, et al. MiR-155 as a diagnostic and prognostic marker in hematological and solid malignancies. *Neoplasma.* 2014;61(3):241–251.
- Sochor M, Basova P, Pesta M, et al. Oncogenic microRNAs: miR-155, miR-19a, miR-181b, and miR-24 enable monitoring of early breast cancer in serum. *BMC Cancer.* 2014;14:448.
- Donnem T, Eklo K, Berg T, et al. Prognostic impact of MiR-155 in non-small cell lung cancer evaluated by in situ hybridization. *J Transl Med.* 2011;9(1):6.
- Slezak-Prochazka I, Kluiver J, de Jong D, et al. Inhibition of the miR-155 target NIAM phenocopies the growth promoting effect of miR-155 in B-cell lymphoma. *Oncotarget.* 2016;7(3): 2391–2400.
- Tili E, Croce CM, Michaille JJ. MiR-155: on the crosstalk between inflammation and cancer. *Int Rev Immunol.* 2009; 28(5):264–284.
- Kim YK, Yu J, Han TS, et al. Functional links between clustered microRNAs: suppression of cell-cycle inhibitors by microRNA clusters in gastric cancer. *Nucleic Acids Res.* 2009;37(5): 1672–1681.
- Van Roosbroeck K, Fanini F, Setoyama T, et al. Combining anti-mir-155 with chemotherapy for the treatment of lung cancers. *Clin Cancer Res.* 2017;23(11):2891–2904.
- Karkare S, Bhatnagar D. Promising nucleic acid analogs and mimics: characteristic features and applications of PNA, LNA, and morpholino. *Appl Microbiol Biotechnol.* 2006;71(5): 575–586.
- Egholm M, Buchardt O, Christensen L, et al. PNA hybridizes to complementary oligonucleotides obeying the Watson-Crick hydrogen-bonding rules. *Nature.* 1993;365(6446):566–568.
- Good L, Nielsen PE. Progress in developing PNA as a gene-targeted drug. *Antisense Nucleic Acid Drug Dev.* 1997;7(4): 431–437.
- Aboul-Fadl T. Antisense oligonucleotides: the state of the art. *Curr Med Chem.* 2005;12(19):2193–2214.
- Shah K, Jacobs A, Breakefield XO, Weissleder R. Molecular imaging of gene therapy for cancer. *Gene Ther.* 2004;11(15): 1175–1187.
- Mukherjee A, Wickstrom E, Thakur ML. Imaging oncogene expression. *Eur J Radiol.* 2009;70(2):265–273.
- Lewis MR, Jia F. Antisense imaging: and miles to go before we sleep? *J Cell Biochem.* 2003;90(3):464–472.
- Tian X, Aruva MR, Qin W, et al. External imaging of CCND1 cancer gene activity in experimental human breast cancer xenografts with [^{99m}Tc]peptide-peptide nucleic acid-peptide chimeras. *J Nucl Med.* 2004;45(12):2070–2082.
- Paudyal B, Zhang K, Chen CP, et al. Determining efficacy of breast cancer therapy by PET imaging of HER2 mRNA. *Nucl Med Biol.* 2013;40(8):994–999.
- Keshavarzi M, Sorayayi S, Jafar Rezaei M, et al. MicroRNAs-based imaging techniques in cancer diagnosis and therapy. *J Cell Biochem.* 2017;118(12):4121–4128.
- Robertson ED, Wasylyk C, Ye T, Jung AC, Wasylyk B. The oncogenic MicroRNA Hsa-miR-155-5p targets the transcription factor ELK3 and links it to the hypoxia response. *PLoS One.* 2014;9(11):e113050.
- Kang L, Huo Y, Ji Q, et al. Noninvasive visualization of microRNA-155 in multiple kinds of tumors using a radiolabeled anti-miRNA oligonucleotide. *Nucl Med Biol.* 2016;43(2): 171–178.
- Zhao X, Wang N, Ren X, et al. Preparation and evaluation of [^{99m}Tc]-epidermal growth factor receptor (EGFR)-peptide nucleic acid for visualization of EGFR messenger RNA expression in malignant tumors. *J Nucl Med.* 2014;55(6):1008–1016.
- Mellis D, Caporali A. MicroRNA-based therapeutics in cardiovascular disease: screening and delivery to the target. *Biochem Soc Trans.* 2018;46(1):11–21.
- Shah P, Bristow MR, Port JD. MicroRNAs in heart failure, cardiac transplantation, and myocardial recovery: biomarkers with therapeutic potential. *Curr Heart Fail Rep.* 2017;14(6): 454–464.
- Thomas KT, Gross C, Bassell GJ. MicroRNAs sculpt neuronal communication in a tight balance that is lost in neurological disease. *Front Mol Neurosci.* 2018;11:455.
- Snowwhite IV, Allende G, Sosenko J, Pastori RL, Cayetano SM, Pugliese A. Association of serum microRNAs with islet autoimmunity, disease progression and metabolic impairment in relatives at risk of type 1 diabetes. *Diabetologia.* 2017;60(8): 1409–1422.
- Subramaniam S, Jeet V, Clements JA, Gunter JH, Batra J. Emergence of microRNAs as key players in cancer cell metabolism. *Clin Chem.* 2019;65(9):1090–1101.
- Mattiske S, Suetani RJ, Neilsen PM, Callen DF. The oncogenic role of miR-155 in breast cancer. *Cancer Epidemiol Biomarkers Prev.* 2012;21(8):1236–1243.
- Tian X, Aruva MR, Qin W, et al. Noninvasive molecular imaging of MYC mRNA expression in human breast cancer xenografts with a [^{99m}Tc]peptide-peptide nucleic acid-peptide chimera. *Bioconjug Chem.* 2005;16(1):70–79.
- Mardirossian G, Lei K, Ruszkowski M, et al. In vivo hybridization of technetium-99m-labeled peptide nucleic acid (PNA). *J Nucl Med.* 1997;38(6):907–913.
- Sun X, Fang H, Li X, Rossin R, Welch MJ, Taylor JS. MicroPET imaging of MCF-7 tumors in mice via unr mRNA-targeted peptide nucleic acids. *Bioconjug Chem.* 2005;16(2):294–305.
- Quijano E, Bahal R, Ricciardi A, Saltzman WM, Glazer PM. Therapeutic peptide nucleic acids: principles, limitations, and opportunities. *Yale J Biol Med.* 2017;90(4):583–598.

33. Dias N, Stein CA. Antisense oligonucleotides: basic concepts and mechanisms. *Mol Cancer Ther.* 2002;1(5):347–355.
34. Oh SY, Ju Y, Kim S, Park H. PNA-based antisense oligonucleotides for microRNAs inhibition in the absence of a transfection reagent. *Oligonucleotides.* 2010;20(5):225–230.
35. Petersen L, de Koning MC, van Kuik-Romeijn P, et al. Synthesis and in vitro evaluation of PNA-peptide-DETA conjugates as potential cell penetrating artificial ribonucleases. *Bioconjug Chem.* 2004;15(3):576–582.
36. Zhang Z, Liu Y, Jarreau C, Welch MJ, Taylor JSA. Nucleic acid-directed self-assembly of multifunctional gold nanoparticle imaging agents. *Biomater Sci.* 2013;1(10):1055–1064.
37. Shen Y, Shrestha R, Ibricevic A, et al. Antisense peptide nucleic acid-functionalized cationic nanocomplex for in vivo mRNA detection. *Interface Focus.* 2013;3(3):20120059.
38. Wang Z, Zhang K, Shen Y, et al. Imaging mRNA expression levels in living cells with PNA-DNA binary FRET probes delivered by cationic shell-crosslinked nanoparticles. *Org Biomol Chem.* 2013;11(19):3159–3167.
39. Vives E. Cellular uptake of the Tat peptide: an endocytosis mechanism following ionic interactions. *J Mol Recognit.* 2003;16(5):265–271.
40. Slivac I, Guay D, Mangion M, Champeil J, Gaillet B. Non-viral nucleic acid delivery methods. *Expert Opin Biol Ther.* 2017;17(1):105–118.